

Supplementary Material for: "Electrically programmable phase-change photonic memory for optical neural networks with nanoseconds in-situ training capability"

Maoliang Wei,^{a,#} Junying Li,^{a,#} Zequn Chen,^{b,c} Bo Tang,^d Zhiqi Jia,^a Peng Zhang,^d Kunhao Lei,^a Kai Xu,^a Jianghong Wu,^{b,c} Chuyu Zhong,^a Hui Ma,^a Yuting Ye,^{b,c} Jialing Jian,^{b,c} Chunlei Sun,^{b,c} Ruonan Liu,^d Ying Sun,^a Wei. E. I. Sha,^a Xiaoyong Hu,^e Jianyi Yang,^a Lan Li,^{b,c} Hongtao Lin^{a,*}

^aState Key Laboratory of Modern Optical Instrumentation, Key Laboratory of Micro-Nano Electronics and Smart System of Zhejiang Province, College of Information Science and Electronic Engineering, Zhejiang University, Hangzhou 310027, China

^bKey Laboratory of 3D Micro/Nano Fabrication and Characterization of Zhejiang Province, School of Engineering, Westlake University, Hangzhou, Zhejiang 310024, China

^cInstitute of Advanced Technology, Westlake Institute for Advanced Study, Hangzhou, Zhejiang 310024, China

^dInstitute of Microelectronics of the Chinese Academy of Sciences, Beijing 100029, China

^eState Key Laboratory for Mesoscopic Physics, Frontiers Science Center for Nano-optoelectronics, School of Physics, Peking University, Beijing 100871, China

M. Wei and J. Li contributed equally to this work.

*Hongtao Lin, hometown@zju.edu.cn

1 Design of the microheater

To electrothermally switch the phase change material Sb_2Se_3 for high-performance modulation, the heating efficiency and waveguide loss of the microheater should be carefully engineered. The PIN diode-embedded waveguide has the same structure as in our previous work[56]. A narrower dope span (S_{dope}) could result in a higher propagation loss (as shown in Fig. S1(a)), whereas the actuation voltage and power consumption can be reduced[58]. Thus, S_{dope} is chosen to be $1.5 \mu\text{m}$ in our design, where the actuation voltage of amorphization was simulated to be 6.0 V for a 500 ns pulse, and the propagation loss of this PIN-diode-embedded waveguide was simulated to be $0.0042 \text{ dB}/\mu\text{m}$. To experimentally characterize the propagation loss, a $20 \mu\text{m}$ -long PIN diode was embedded in a microring resonator and the propagation loss could be extracted. The manufactured PIN diode embedded microring resonator's normalized transmission spectrum and Lorentz fitted result are shown in Fig. S1(b), and the corresponding Q-factor is 14193, which yields a propagation loss of 6.8 dB/cm. After deducting the propagation loss induced by the bare silicon waveguide[59], the

propagation loss of the PIN-doped silicon waveguide could be determined, corresponding to a loss of 0.0065 dB/ μm .

The metal span can be further reduced to lower the drive voltage. We have established in our earlier work that the propagation loss is ignorable when the metal span is more than 2 μm [56]. Thus, by decreasing the metal span (the distance between the waveguide core and the metal) decrease from 5 μm to 2 μm , the actuation voltage can theoretically be reduced to 3.3 V (See Fig. S1(c)).

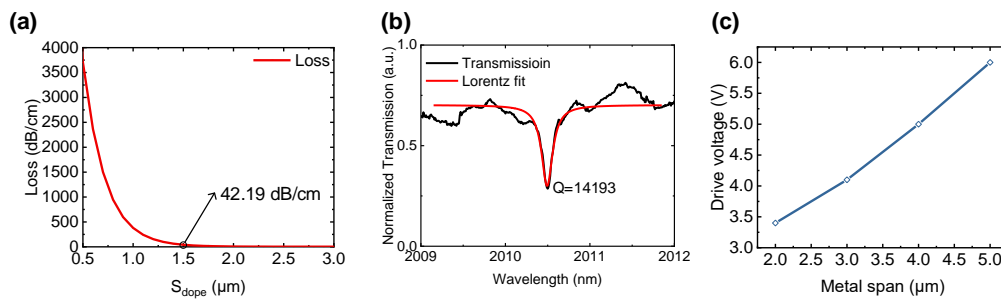


Fig. S1 Design of the microheater. (a) Loss induced by doped silicon decreases with the dope span (S_{dope}) between the p-type doped region and the n-type doped region. (b) Normalized transmission spectrum (black line) and the Lorentz fitted result (red line) of the resonance peak at 2010.49 nm. (c) Change of actuation voltage for amorphization with different metal spans. (The pulse duration is 500 ns for each voltage pulse.)

2 Analysis of volatile modulation compatibility of the photonic memory

The PIN diode in the PCM-integrated photonic memory allows realizing volatile modulation by leveraging the free carrier dispersion of silicon, as long as the forward bias applied is kept below a threshold to ensure that the thermo-optic effect does not dominate the volatile modulation.

Joule heating of a PIN diode is inevitable when a forward bias is applied, and the refractive index of silicon is simultaneously affected by the carrier injection and the temperature both inside/outside the silicon waveguide core. Note that the carrier injection of silicon decreases the effective refractive index (n_{eff}) of waveguides, whereas

heating up the waveguides does the opposite. COMSOL simulation was conducted to maximize the free carrier effect induced modulation in a 20- μm PIN-diode embedded waveguide. The n_{eff} of the PIN-doped waveguide reached its minimum (i.e. $2.22356 - i0.00226$) at the bias current of 5.84 mA (see Fig. S2 (a)), and further increasing the bias voltage led to the thermo-optic effect. The temperature distribution of the waveguide region suggests that the temperature of the waveguide is lower than 355 K at the bias current of 5.84 mA (as shown in Fig. S2 (b)), far below the temperature needed for phase transition SbSe, typically 473 K for crystallization. This confirms the compatibility of the PCM-driven photonic memory with volatile modulation.

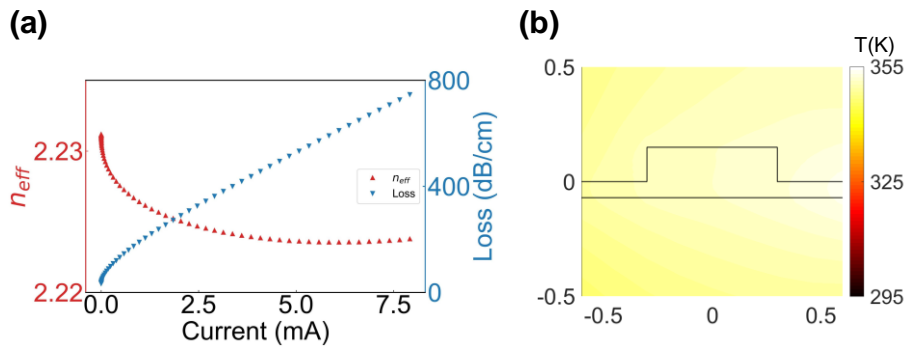


Fig. S2 Mechanism of the volatile modulation. (a) Effective refractive index and propagation loss of 20- μm PIN diode embedded waveguide. (b) Simulated temperature profile of the PIN diode at 5.84 mA.

3 The measurement setup

Fig. S3 shows the measurement setup. Signal light from a 2- μm tunable laser (Laser) was sent into a polarization controller (PC) and then coupled into/out from the device under test (DUT) by two grating couplers. An arbitrary waveform generator (AWG) was employed to generate voltage pulses applied to the DUT via an RF probe, controlling the volatile modulation and phase switching of PCM-integrated photonic memory. The output light from the DUT was detected by a photodetector (PD) and the analog signals were collected by a data acquisition equipment (DAQ).

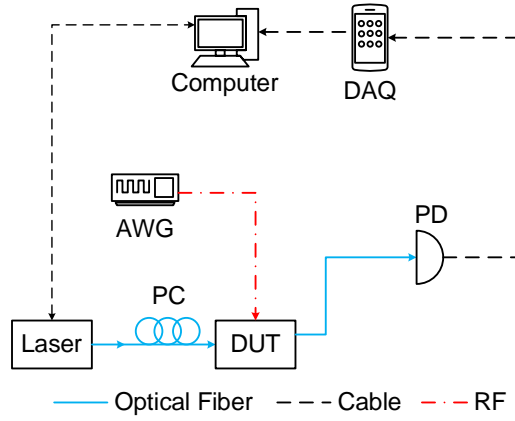


Fig. S3 The measurement setup. DAQ: data acquisition equipment, AWG: arbitrary waveform generator, PD: photodetector, Laser: the tunable laser, DUV: device under test.

4 Low-actuation-voltage PCM-based photonic memory

The concentrated Joule heat of the PIN diode underneath SbSe makes heating more efficient, thus reducing power consumption. Here, by reducing the spacing gap between the waveguide core and the metal electrode (S_{metal}) from 5 μm to 2.1 μm , we demonstrated that the amorphization drive voltage decreased from 8.2 V to 6.4 V during the amorphization process when the same pulse duration (500 ns) was employed. Fig. S4 (a) shows the change of transmittance spectra of the device resulting from the reversible switching, where the amorphization was achieved with a 6.4 V/500 ns pulse and the crystallization was realized with a 2.6 V/1 ms pulse. Furthermore, by increasing the pulse duration to 2 μs , the minimum driving voltage for the amorphization of SbSe was reduced to 4.4 V, as shown in Fig. S4 (b).

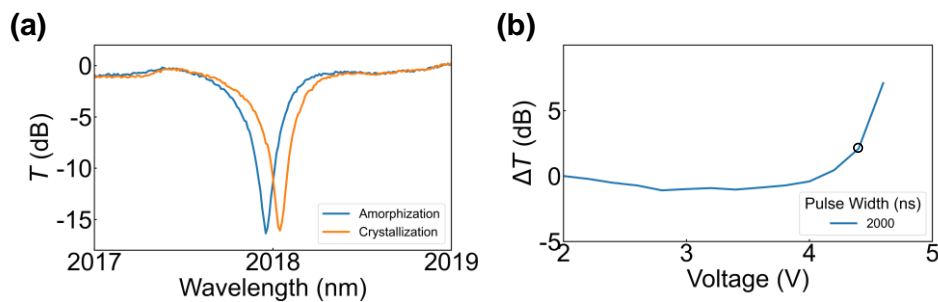


Fig. S4 Lowering the drive voltage of photonic memory down to <5 V by reducing waveguide-and-electrode spacing and prolonging the pulse duration. (a) Measured transmittance spectra of a microring

resonator photonic memory with the S_{metal} narrowed to 1.1 μm . (b) Change of transmission with the actuation voltage when increasing the amorphization pulse duration to 2 μs .

5 The scalability of photonic memory

In on-chip ONNs, to avoid crosstalk between wavelength multiplexing channels, the wavebands of each photonic memory should be separated. Here we constructed the 4×4 OCK, since the large radius of MRR leads to a limited free spectral range (FSR) of 4.2 nm. The maximum occupied band of a crystalline Sb_2Se_3 -MRR is 1 nm, as shown in Fig. S5. The occupied wavelength bands are 1 nm ($\Delta\lambda_1 = 0.45$ nm, $\Delta\lambda_2 = 0.30$ nm, $\Delta\lambda_3 = 0.25$ nm) for volatile modulation and 0.73 nm ($\Delta\lambda_4 = 0.31$ nm, $\Delta\lambda_5 = 0.17$ nm, $\Delta\lambda_6 = 0.25$ nm) for non-volatile one. However, compacter micro ring resonators can easily expand the FSR and decrease the full width at half maximum (FWHM) of resonant peaks, thus scaling up the photonic-memory-embedded ONNs. As shown in Table S1, there is no extra propagation loss for the MRR with a radius of 8 μm , and the corresponding FSR of the MRR is 21 nm, which, in principle, can support 21 channels of optical signals.

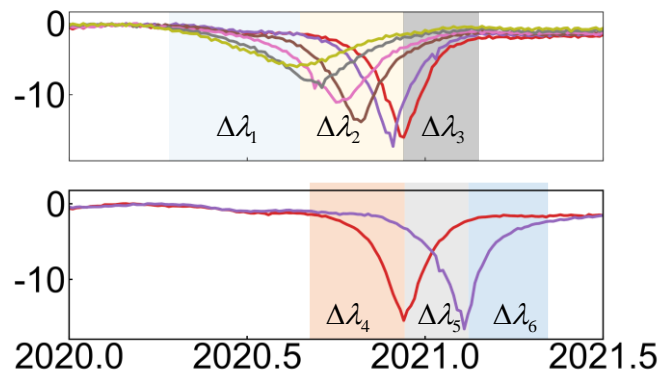


Fig. S5 The occupied bands of the volatile and non-volatile modulation.

Table S1 The increase of channel number with the decrease of the radius of Sb₂Se₃-MRR.

Radius of MRR (μm)	Bending loss (dB/cm)	n_g at 2025 nm	FSR (nm)	Channel number
10	0	3.759	17.36	17
9	0	3.757	19.30	19
8	0	3.756	21.71	21
7	1.64	3.753	24.84	24
6	6.34	3.750	29.01	29

6 The influence of multi-bit storage on ONNs

An ONN with 4×4 OCK was simulated, and the schematic diagram is shown in Fig. S6 (a). The whole linear network of the ONN was constructed from the photonic memories. The ONN was trained to identify the MNIST data set, making an accurate prediction with a 94.64% accuracy rate (See Fig. S6 (b)). Then, the trained weights of the whole linear network were written into various bits of photonic memory ranging from 1 to 5 bits to obtain the tested confusion matrix (see Fig. S6 (c-g)). By storing the trained weights in a 4-bits photonic memory, an average prediction accuracy of 94.50% was attained, which is comparable with the trained one. While the bits are reduced to 3, the accuracy is lower than 94%. Therefore, we have verified that a 4-bit photonic memory is capable of supporting the identification of the MNIST data set. For more complicated applications, >5-bit photonic memories are expected.

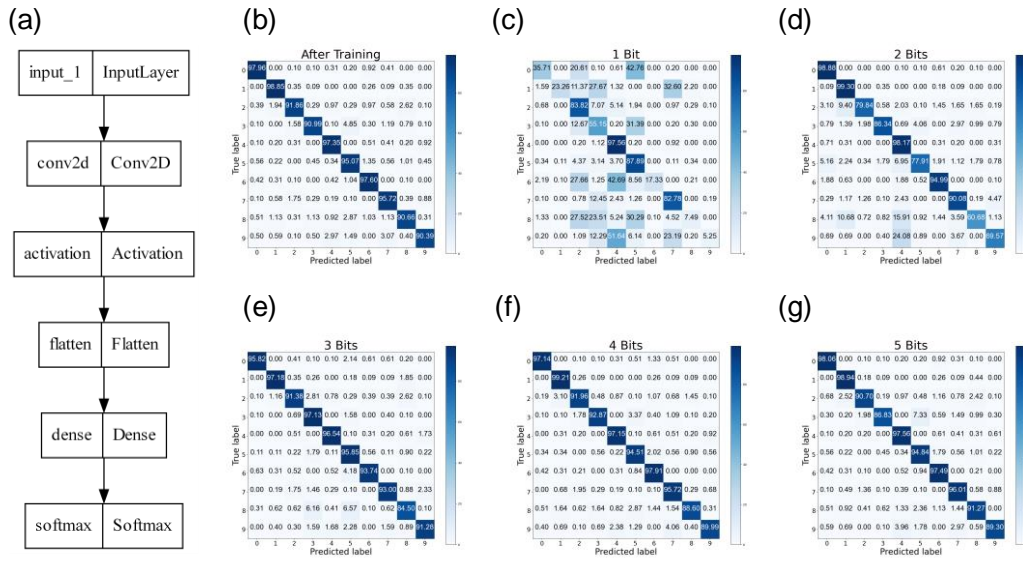


Fig. S6 Influence of multi-bit storage on MNIST handwriting recognition by an ONN with a 4×4 OCK.

(a) Schematic diagram of the simulated ONN. (b) Tested confusion matrix after in-situ training. Predicted results after writing to photonic memory in 1 bit (c), 2 bits (d), 3 bits (e), 4 bits (f), and 5 bits (g).